# Computation & theory

# Performance of hybrid functional in linear combination of atomic orbitals scheme in predicting electronic response in spinel ferrites ZnFe$_2$O$_4$ and CdFe$_2$O$_4$

N. L. Heda[1,*] (iD), Kalpana Panwar[1], Kishor Kumar[2], and B. L. Ahuja[2]

[1] Department of Pure and Applied Physics, University of Kota, Kota, Rajasthan 324005, India
[2] Department of Physics, M.L. Sukhadia University, Udaipur, Rajasthan 313001, India

## ABSTRACT

Pure and hybrid density functional theory (DFT) schemes within linear combination of atomic orbitals (LCAO) have been employed to compute Mulliken population (MP), energy bands, density of states (DOS) and electron momentum densities (EMDs) of TMFe$_2$O4 (TM = Zn and Cd). Pure DFT calculations were performed within local density and generalized gradient approximations, while Hartree–Fock exchange contribution is added to DFT for hybrid calculations (B3LYP and PBE0). To validate the performance of hybrid functionals, we have also performed EMD measurements using 661.65 keV $\gamma$-rays from $^{137}$Cs source. Chi-square test predicts an overall better agreement of experimental Compton profile data with LCAO–B3LYP scheme-based momentum densities leading to usefulness of hybrid functionals in predicting electronic and magnetic response of such ferrites. Further, LCAO–B3LYP-based majority- and minority-spin energy bands and DOS for ZnFe$_2$O$_4$ and CdFe$_2$O$_4$ predict semiconducting nature in both the compounds. In addition, MP data and equal-valence-electron-density scaled EMDs show more covalent character of ZnFe$_2$O$_4$ than that of CdFe$_2$O$_4$. A reasonable agreement of magnetic moments of both the ferrites with available data unambiguously promotes use of Gaussian-type orbitals in LCAO scheme in exploring magnetic properties of such ferrites.

## Introduction

Zinc and cadmium ferrites (ZnFe$_2$O$_4$ and CdFe$_2$O$_4$) crystallize in cubic spinel structure and are classified as important functional materials due to their peculiar electronic and magnetic properties [1–4]. Regarding earlier studies, Evans et al. [1] have employed

Mössbauer spectroscopy (MS) to calculate nuclear quadrupole coupling constants and isomer shifts. Temperature-dependent electric-field gradients of both the ferrites were studied using time differential perturbed angular correlation technique by Pasquevich and Shitu [2]. Further, density functional theory (DFT) with generalized gradient approximation

Address correspondence to E-mail: nlheda@yahoo.co.in

https://doi.org/10.1007/s10853-019-04289-8

(GGA) and GGA plus one side Coulomb interaction (GGA + U) schemes were applied to highlight Fe–Fe interactions [3]. DFT within local density approximation (LDA), GGA, LDA + U and GGA + U schemes were employed by Cheng and Liu [4] to discuss the cation distribution effect in both the compounds. Electronic and magnetic properties of $ZnFe_2O_4$ were reported using DFT schemes with different approximations, namely atomic-sphere approximations [5], general potential linearized augmented plane wave method (LAPW) [6], plane wave pseudopotential (PWP) [7] and full potential (FP)-LAPW [8]. On the experimental side, structural and magnetic properties of $ZnFe_2O_4$ were explored by neutron diffraction, MS, X-ray diffraction (XRD), scanning electron microscopy, energy dispersive spectroscopy, vibrating sample magnetometer and Fourier transform infrared (FTIR) measurements [9–11]. Also, Quintero et al. [12, 13] have studied $ZnFe_2O_4$ using FP-LAPW method and MS measurements to visualize effect of defects on structural, electronic, hyperfine and magnetic properties. In case of $CdFe_2O_4$, Mahmood et al. [14] have used DFT with Perdew–Becke–Ernzerhof (PBE) revised for solids (PBESol) with modified Becke–Johnson (mBJ) exchange–correlations potentials to explain optical, magnetic and thermoelectric properties. Measurements on $CdFe_2O_4$ which include XRD, electrical conductivity, thermoelectric power, magnetic hysteresis, initial magnetic susceptibility, infrared spectroscopy and MS, inelastic neutron scattering and structural and transport properties have been reported by different groups [15–17]. In addition, density of states (DOS) along with optical and X-ray magnetic circular dichroism properties of $CdFe_2O_4$ were discussed by Zaari et al. [18] using FP-LAPW-DFT with mBJ potentials.

It is well known that Compton scattering (CS) measurements can be uniquely applied in testing various exchange–correlation potentials through electron momentum densities (EMDs) [19, 20]. The projection of EMD along the z-axis (scattering vector direction) is measured in CS experiment and is defined as Compton profile (CP), $J(p_z)$. Mathematically,

$$J(p_z) = \int\limits_{p_x=-\infty}^{+\infty} \int\limits_{p_y=-\infty}^{+\infty} \rho(\vec{p_x}, \vec{p_y}, \vec{p_z}) \mathrm{d}\vec{p_x} \mathrm{d}\vec{p_y} \qquad (1)$$

Here, $\rho(\vec{p_x}, \vec{p_y}, \vec{p_z})$ represents the momentum distribution of the electrons while $\vec{p_x}, \vec{p_y}$ and $\vec{p_z}$ are the

components of electron linear momentum ($\vec{p}$) along x-, y- and z-directions of the Cartesian coordinate system. Experimentally, we deduce CP from the measured double differential Compton cross section using the relations,

$$J(p_z) = \frac{\text{Double differential Compton cross-section}}{C(E_1, E_2, \theta, p_z)} \qquad (2)$$

Here, $C(E_1, E_2, \theta, p_z)$ depends on the experimental setup with $E_1$ and $E_2$ being the incident and scattered energies of photons and $\theta$ is the photon scattering angle. The variable $C$ in Eq. 2 depends on the experimental geometry also.

In the present work, we have employed CRYSTAL14 code [21] to compute Mullikan population (MP), energy bands, DOS and CPs for $TMFe_2O_4$ (TM = Zn and Cd). The purpose of present CP measurements is hands-on validation of various types of exchange and correlation potentials and hybrid functionals for reliable electronic properties under the frame work of linear combination of atomic orbitals (LCAO). We have also scaled the experimental and theoretical CP on equal-valence-electron-density (EVED) to predict a relative nature of bonding in these iso-electronic compounds. Furthermore, trend of bonding in both the ferrites has also been validated by the present MP analysis. Going beyond CPs, energy bands, DOS, band gaps and magnetic moments of both the compounds have been compared with the available data which enables to conclude about applicability of different types of exchange–correlation energy and hybrid schemes in such type of ferrites.

## Methodologies

### Theory

LCAO calculations have been performed within the hypothesis of DFT and hybridizations of Hartree–Fock (HF) to DFT (so called B3LYP and PBE0) as embodied in the CRYSTAL14 software [21]. We have adopted the LDA and GGA under the DFT scheme. In LCAO calculations, one solves the one electron Schrodinger equation ($\hat{H}\psi = E\psi$) to obtain the crystal wave functions. The Hamiltonian energy operator ($\hat{H}$) includes kinetic energy, electrostatic potential

(arising due to interaction of nuclei with electrons), electrostatic repulsion between electrons and exchange–correlation density functional energy ($E_{XC}$). First three part of $\hat{H}$ are same in DFT–LDA, DFT–GGA, B3LYP and PBE0 approximations, whereas differences among these approximations occur in terms of $E_{XC}$. In case of DFT within LDA or GGA, $E_{XC}$ is defined as,

$$E_{XC}^{\text{LCAO-DFT-LDA/GGA}}\{n(\vec{r})\} = \int n(\vec{r})\varepsilon_{xc}\{n(\vec{r})/(n(\vec{r}), |\nabla n(\vec{r})|)\}d\vec{r} \tag{3}$$

In Eq. 3, $\varepsilon_{xc}$ is known as exchange–correlation energy per particle in uniform electron gas and n($\vec{r}$) is the electron density. In case of LCAO–DFT–LDA scheme, we have adopted exchange and correlation potentials of Dirac-Slater [21] and Perdew and Zunger [22], respectively. While the exchange and correlation energies of PBESol [23] were considered for LCAO–DFT–GGA approximations. In case of hybridized (HF + DFT) approximations (B3LYP and PBE0), $E_{XC}$ is defined as:

$$E_{XC}^{\text{LCAO-B3LYP}} = A * E_X^{\text{LDA}} + B * \Delta E_X^{\text{BECKE}} + (1 - A) * E_X^{\text{HF}} + C * E_C^{\text{LYP}} + (1 - C) * E_C^{\text{VWN}} \tag{4}$$

$$E_{XC}^{\text{LCAO-PBE0}} = D * E_X^{\text{HF}} + (1 - D) * E_X^{\text{PBE}} + E_C^{\text{PBE}} \tag{5}$$

The standard values of $A$, $B$, $C$ and $D$ are 0.80, 0.72, 0.81 and 0.25, respectively [24, 25]. Further $E_X^{\text{HF}}$, $E_X^{\text{LDA}}$, $E_X^{\text{BECKE}}$ and $E_X^{\text{PBE}}$ are the exchange energies corresponding to HF [21], Dirac-Slater [21], Becke [26] and Perdew et al. [27]. $E_C^{\text{LYP}}$, $E_C^{\text{VWN}}$ and $E_C^{\text{PBE}}$ are the correlation energies of Lee et al. [28], Vosko et al. [29] and Perdew et al. [27], respectively.

Further, all electron basis sets of Zn, Cd, Fe and O atoms [30] were used after the re-optimization for the lowest energy of both the ferrites using BILLY code [21]. The lattice parameters, position of atoms and space group of spinel $ZnFe_2O_4$ and $CdFe_2O_4$ were adopted from Quintero et al. [13] and Zaari et al. [18], respectively. The self-consistent field (SCF) calculations for both the compounds were performed with 29 **k** points in the irreducible Brillouin zone (BZ). The unit cell in cubic spinel structure for $ZnFe_2O_4$ is plotted using XCrysden visualization software of Kokalj [31] (Fig. 1a) and the corresponding first BZ structure is sketched in Fig. 1b.

## Experiment

To ratify the choice of exchange and correlation potentials through reconciliation of theoretical and experimental CPs, we have employed 20 Ci [137]Cs Compton spectrometer [32] to measure CPs of $TMFe_2O_4$ (TM = Zn and Cd). In the present measurements, an absolute momentum resolution (Gaussian full width at half maximum) of the experimental setup was 0.34 a.u. Due to difficulties in growing large size single crystals (15 mm diameter and 2 mm thickness) and to discuss the relative nature of bonding on EVED scale of $ZnFe_2O_4$ and $CdFe_2O_4$, we have taken pallets of high purity (> 99%) polycrystalline powder of both the ferrites. Further, γ-radiations of energy 661.65 keV were allowed to incident on pallets of individual ferrite and the scattered radiations (160 ± 0.6° scattering angle) were energy analyzed by a high purity Ge detector (GL0510P, Canberra made). During the exposure time of 162.4 (273.8) h for $ZnFe_2O_4$ ($CdFe_2O_4$), the integrated Compton intensity was found to be $3.17 \times 10^7$ ($4.44 \times 10^7$) counts. The stability of the acquisition system was monitored from time-to-time by two weak radio-isotopes, namely [57]Co and [133]Ba. To obtain absolute CP, the raw Compton spectra of both the ferrites were corrected for systematic corrections (background, detector efficiency, sample absorption, stripping-off the low energy tail and CS cross section) with computer code of Warwick group [33]. To obtain true singly scattered photon profile, we have also corrected the data for the effect up to triple scattering using Monte Carlo method [34]. Each Compton line was normalized to corresponding free atom (FA) CP area using the tabulated values of Biggs et al. [35]. The value of FA CP area for $ZnFe_2O_4$ ($CdFe_2O_4$) was 51.62 (57.77) $e^-$ in the momentum range 0–7 a.u.

## Results and discussion

### MP analysis

MP data of charge transfer for $TMFe_2O_4$ (TM = Zn and Cd) using LCAO–DFT–LDA, LCAO–DFT–GGA, LCAO–B3LYP and LCAO–PBE0 schemes have been presented in Table 1. Here, the transition metal atoms (Zn/Cd and Fe) in $TMFe_2O_4$ (TM = Zn/Cd) donate charge to the oxygen atoms and total charge from

**Figure 1** Structural sketch of **a** ZnFe$_2$O$_4$ plotted using software tool of Kokalj [31]. For CdFe$_2$O$_4$ structure, Zn is replaced by Cd. **b** First BZ corresponding to structural sketch given in part '**a**'.
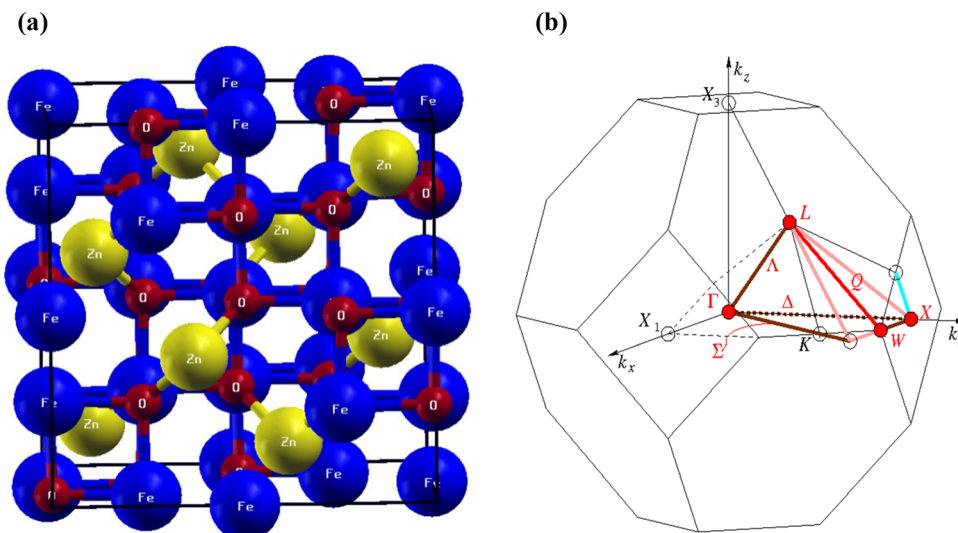


donor is equally distributed among O atoms for both the compounds. The total numerical values of charge transfer in ZnFe$_2$O$_4$ (CdFe$_2$O$_4$) are 4.12 (4.32), 4.16 (4.40), 4.44 (4.60) and 4.52 (4.72) $e^-$ using LCAO–DFT–LDA, LCAO–DFT–GGA, LCAO–B3LYP and LCAO–PBE0 schemes, respectively. It is observed that the charge transfer in CdFe$_2$O$_4$ is higher than that in ZnFe$_2$O$_4$ for each approximation (LCAO–DFT–LDA/LCAO–DFT–GGA/LCAO–B3LYP/LCAO–PBE0). Such trend of MP data indicates more ionic (or less

**Table 1** Mulliken's population (MP) data for TMFe$_2$O$_4$ (TM = Zn and Cd) using LCAO–DFT–LDA, LCAO–DFT–GGA, LCAO–B3LYP and LCAO–PBE0 schemes as mentioned in the text

| Scheme | Amount of charge transfer ($e^-$) | | |
|---|---|---|---|
| | Donor atoms | | Acceptor atoms |
| | Zn/Cd (2) | Fe (4) | O (8) |
| (a) ZnFe$_2$O$_4$ | | | |
| LCAO–DFT–LDA | 1.04 | 1.54 | 1.03 |
| LCAO–DFT–GGA | 1.06 | 1.55 | 1.04 |
| LCAO–B3LYP | 1.16 | 1.64 | 1.11 |
| LCAO–PBE0 | 1.18 | 1.67 | 1.13 |
| (b) CdFe$_2$O$_4$ | | | |
| LCAO–DFT–LDA | 1.18 | 1.57 | 1.08 |
| LCAO–DFT–GGA | 1.22 | 1.59 | 1.10 |
| LCAO–B3LYP | 1.30 | 1.65 | 1.15 |
| LCAO–PBE0 | 1.32 | 1.70 | 1.18 |

Here, TM (Zn and Cd) and Fe atoms are the donor atoms while O atoms are the acceptor atoms. The numbers of equivalent atoms are shown in the brackets

covalent) character in CdFe$_2$O$_4$ than that in ZnFe$_2$O$_4$, as larger value of charge transfer in any compound reflects more ionicity. Also, in all the adopted approximations, contribution of Fe atom in total charge transfer data is found to be approximately similar for both the compounds. However, difference in total charge transfer exists due to the contribution of Zn/Cd atom in TMFe$_2$O$_4$ environment. In addition to MP data for charge transfer, we have also calculated overlap population (OP) between the nearest neighbor atoms in both the compounds. The OP value of identical Fe–O in TMFe$_2$O$_4$ (TM = Zn/Cd) are found to be 0.051, 0.051, 0.049 and 0.048 $e^-$ using LCAO–DFT–LDA, LCAO–DFT–GGA, LCAO–B3LYP and LCAO–PBE0, respectively, for both the compounds. While these values for Zn–O (Cd–O) in case of ZnFe$_2$O$_4$ (CdFe$_2$O$_4$) are observed as 0.127 (0.047), 0.126 (0.045), 0.124 (0.039) and 0.120 (0.035) $e^-$ using LCAO–DFT–LDA, LCAO–DFT–GGA, LCAO–B3LYP and LCAO–PBE0, respectively. The OP values of Zn–O in case of ZnFe$_2$O$_4$ are higher than that for Cd–O in CdFe$_2$O$_4$ using all the LCAO approximations. It indicates more covalent (or less ionic) character of ZnFe$_2$O$_4$ than that in CdFe$_2$O$_4$ because large value of OP indicates more covalent character of the compound. It is worth mentioning that MP analysis of charge transfer is bound to be quite reliable as we have included large number of atomic orbitals in each LCAO computation using DFT–LDA, DFT–GGA, B3LYP and PBE0 prescriptions. Such MP analysis have successfully been reported in various other oxides, viz. TMWO$_4$ (TM = Co, Ni, Cu, Zn and Cd)

[36, 37], $Ag_2TMO_4$ (TM = Cr and Mo) [38] and $BaTiO_3$ [39].

## Energy bands and density of states

Majority (spin-up) and minority (spin-down) energy bands of LCAO–B3LYP scheme are presented in Figs. 2 and 3 for $ZnFe_2O_4$ and $CdFe_2O_4$, respectively. Except some fine structures, the energy bands of LCAO–B3LYP are in consonance with LCAO–DFT–LDA, LCAO–DFT–GGA and LCAO–PBE0 schemes; hence, energy bands are shown only for B3LYP scheme (which performed well in reproducing EMDs, as discussed later). Also, our energy bands of $ZnFe_2O_4$ and $CdFe_2O_4$ reasonably resemble with the available data [6, 7, 14]. From Figs. 2 and 3, a significant energy gap between the valence band maximum (VBM) and conduction band minimum (CBM) is observed in both the majority- and minority-spin channels of both the compounds. Present band structures indicate a direct band gap ($E_g$) semiconducting nature of $ZnFe_2O_4$ and $CdFe_2O_4$, as VBM and CBM are found at the same $\Gamma$ point. The band gap values for both the compounds are lower in case of minority-spin bands channels than that in majority-spin channel (Figs. 2, 3). In Table 2, we have collated band gap values derived using various approximation (LCAO–DFT–LDA, LCAO–DFT–GGA, LCAO–B3LYP and LCAO–PBE0) along with available theoretical and experimental data [7, 12–14, 18, 40–42] for $TMFe_2O_4$. Our band gap values using LCAO–DFT–

LDA and LCAO–DFT–GGA schemes underestimate the experimental band gap [40–42] for both the compounds, while a reverse trend is found for LCAO–B3LYP and LCAO–PBE0 schemes. It is seen that B3LYP approach shows a closer agreement with the experimental band gap than other schemes considered within the periphery of LCAO prescription. It is worthwhile to mention that most of the theoretical prescriptions using pure LDA and GGA schemes have underestimated the band gap values than the experimental band gaps, as evident from Table 2. This trend is consistent with the general observation that the HF calculations overestimate the band gap (because of lack of screening in the exchange term leading to an over stabilization of occupied states) and the DFT-based LDA and GGA theories underestimate the band gap. It is quite satisfying that in this situation the hybrid method (mixing of HF to DFT) like B3LYP minimizes the deviation of band gap from the experimental values and leads to reasonable electronic response for such compounds.

In Fig. 4a–d, we have shown DOS for spin-up (↑) and spin-down (↓) states using LCAO–B3LYP scheme for $3d$, $4s$ states of Zn; $3d$, $4s$ states of Fe; $2s$, $2p$ states of O and total DOS for $ZnFe_2O_4$. Similarly, spin-projected DOS for $CdFe_2O_4$ environment are plotted in Fig. 5a–d. The Fermi energy ($E_F$) is shifted to 0 eV. The majority-spin and minority-spin DOS for both the compounds unambiguously reconfirm the semiconducting nature of both the compounds. In Fig. 4 (Fig. 5), the DOS in energy range − 8.34
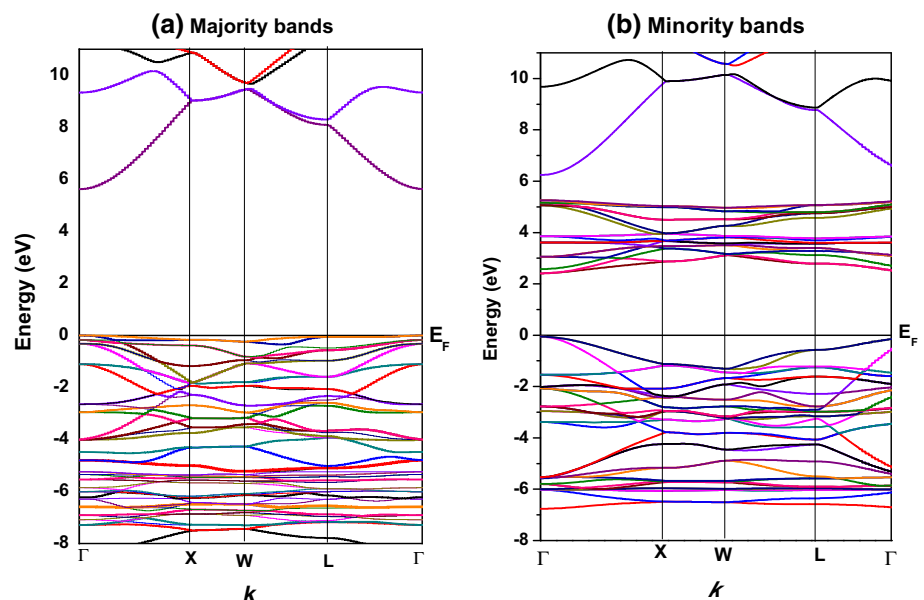
Figure 2 **a** Majority- and **b** minority-spin energy bands of $ZnFe_2O_4$ using LCAO–B3LYP scheme along the high symmetry directions of BZ. The positions of $\Gamma$, $X$, $W$ and $L$ vertices are (0, 0, 0), (1/2, 0, 1/2), (1/2, 1/4, 3/4) and (1/2, 1/2, 1/2), respectively.
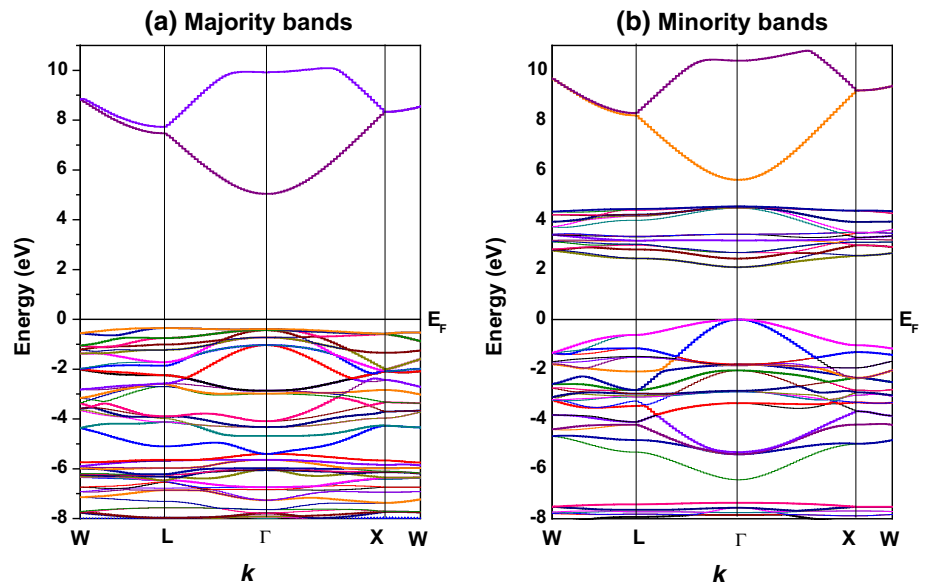
**Figure 3** **a** Majority- and **b** minority-spin energy bands of $CdFe_2O_4$ using LCAO–B3LYP scheme along the high symmetry directions of BZ.



(− 8.65) eV to the $E_F$ level are mostly contributed by the 3*d* (4*d*) electrons of Zn (Cd) and 3*d* electrons of Fe atom along with a small contribution of 2*p* electrons of O atoms. In Fig. 4d, the majority-spin states dominate in the formation of the DOS in the energy range − 8.34 to − 6.77 eV, while the DOS in the energy range + 2.40 to + 5.23 eV are majorly contributed by the minority-spin states of $ZnFe_2O_4$. In case of $CdFe_2O_4$ (Fig. 5d), contribution of minority-spin (majority-spin) DOS are found to be absent in the energy range − 7.36 to − 6.46 (+ 2.10 to + 4.52) eV. In Fig. 4a, the majority-spin DOS of Zn-3*d* states are dominated in the energy range − 8.34 to − 6.60 eV while the trend becomes reverse and dominancy of minority-spin DOS of 3*d* states of Zn prevails between − 6.60 and − 5.53 eV. Similarly, major role of majority-spin states of Fe is found between the energy range − 8.34 to − 3.30 eV (Fig. 4b). In the conduction band region between + 2.40 and + 5.23 eV, the DOS are majorly governed by 3*d* minority-spin states of Fe atom along with a small contribution of minority-spin states of 2*p* electrons of O atom (Fig. 4b, c). In Fig. 5a, major contribution of majority-spin states of 4*d* electrons of Cd is seen between − 8.65 and − 7.89 eV and a reverse trend is observed between − 7.89 and − 7.38 eV. For 3*d* electrons of Fe (Fig. 5b), the majority-spin contribution dominates in the valence band region (− 8.65 to − 0.36 eV) and minority-spin contribution dominates in conduction band region (+ 2.10 to + 4.52 eV) of $CdFe_2O_4$. From Fig. 4c for $ZnFe_2O_4$ and Fig. 5c for

$CdFe_2O_4$, a small contribution below the VBM is found from majority- and minority-spin states of O, while the contribution of only minority-spin states of O atoms in CBM is witnessed. It is observed that the VBM is formed by the majority-spin states of 3*d* (4*d*) of Zn (Cd) and 3*d* states of Fe along with the a small contribution of majority-spin O-2*p* states for $ZnFe_2O_4$ ($CdFe_2O_4$). Also, the CBM is built mainly by minority-spin of 3*d* (4*d*) states of Fe along with a small contribution of minority-spin of 2*p* states of O atom in $ZnFe_2O_4$ ($CdFe_2O_4$).

## Compton profiles

In Fig. 6a, b, the anisotropies between unconvoluted theoretical CPs ($J_{110}$–$J_{100}$, $J_{111}$–$J_{100}$ and $J_{111}$–$J_{110}$) using LCAO–DFT–LDA, LCAO–DFT–GGA, LCAO–B3LYP and LCAO–PBE0 schemes are presented for $ZnFe_2O_4$ and $CdFe_2O_4$, respectively. An overall trend of oscillations in the anisotropies ($J_{110}$–$J_{100}$, $J_{111}$–$J_{100}$ and $J_{111}$–$J_{110}$) for $TMFe_2O_4$ (TM = Zn and Cd) using LCAO computations (DFT–LDA, DFT–GGA, B3LYP and PBE0) are found to be similar. In the higher momentum region ($p_z \geq 4.0$ a.u.), negligible anisotropic effects in momentum densities of both the compounds have been observed for all the considered schemes (LCAO–DFT–LDA, LCAO–DFT–GGA, LCAO–B3LYP and LCAO–PBE0). In high momentum region, such observations are quite expected as core electrons which contribute to formation of CPs in this region remain unaffected in directional momentum densities. Anisotropic effects are observed in the low

**Table 2** Band gap ($E_g$) for $ZnFe_2O_4$ and $CdFe_2O_4$ using various combinations of exchange–correlation potentials within LCAO schemes as mentioned in the text along with the available data

| Approach | Band gap ($E_g$) in eV | |
|---|---|---|
| | $ZnFe_2O_4$ | $CdFe_2O_4$ |
| (i) Present computations | | |
| LCAO–DFT–LDA | 1.06 | 0.52 |
| LCAO–DFT–GGA | 1.37 | 0.40 |
| LCAO–B3LYP | 2.40 | 2.10 |
| LCAO–PBE0 | 3.22 | 3.26 |
| (ii) Available theories | | |
| (a) Plane wave pseudopotential (PWP) [7] with | | |
| LDA-CA-PZ | 0.87 | – |
| GGA–PBE | 0.84 | – |
| GGA–RPBS | 0.93 | – |
| GGA–PW91 | 0.79 | – |
| GGA–WC | 0.87 | – |
| GGA–PBESOL | 0.80 | – |
| (b) FP-LAPW + lo [12] | 2.20 | – |
| (c) FP-LAPW + lo with GGA + U [13] | | |
| Non inverted | 2.00 | – |
| Inverted | 2.10 | – |
| (d) Projector-augmented wave (PAW) [40] with | | – |
| GGA + U (spinel) | 1.68 | – |
| PBE0 (spinel) | 3.68 | – |
| GGA + U (inverse) | 1.91 | – |
| PBE0 (inverse) | 3.37 | – |
| (e) FP-LAPW with PBESOL + mBJ [14] | – | 1.86 |
| (f) FP-LAPW–DFT [18] with | | |
| GGA + U | – | 1.56 |
| TB-mBJ | – | 1.88 |
| (iii) Available experiment | | |
| Yao et al. [7] | 1.90 | – |
| Valeznuela et al. [41] | 1.92 | – |
| Akamatsu et al. [42] | – | 1.46 |

momentum region ($p_z \leq 4.0$ a.u.), which are dictated by dispersive nature of energy bands and their degeneracy in different branches of BZ. In low momentum side, the trend of anisotropies in hybrid schemes (LCAO–B3LYP and LCAO–PBE0) is almost similar, while it differs from the overall trend seen for LCAO–DFT–LDA and LCAO–DFT–GGA schemes. Such a trend in hybrid calculations may be due to the incorporation of HF exchange energy component in B3LYP and PBE0 schemes, which was absent in DFT with LDA and GGA. As expected, the oscillations in CP anisotropies in Fig. 6a–b are also in consonance with the cross-overs and degenerate states of majority- and minority-spin energy bands (Figs. 2, 3) for both the compounds. The positive values of anisotropies ($J_{111}$–$J_{100}$ and $J_{111}$–$J_{110}$) in Fig. 6a, b near $p_z = 0.0$ a.u. are due to the large degenerate states along [111] direction as compared to [100] and [110] directions. Decreasing order of $J(p_z = 0.0$ a.u.) values for the three crystallographic directions is found to be [111] → [110] → [100] for both the compounds which shows signatures of atomic density effects in different principal orientations. Also, the negative amplitude near $p_z = 1.5$ a.u. along $J_{111}$–$J_{100}$ in Fig. 6a, b arises due to zone boundary of $\Gamma$–$X$ (0.39 a.u.; $n = 4$ for $ZnFe_2O_4$ and 0.38 a.u.; $n = 4$ for $CdFe_2O_4$) branch. It may be noted that some fine structures may be invisible in the anisotropies (Fig. 6) because of cancellation effect on taking the differences of CPs. Anisotropic measurements of CPs for $ZnFe_2O_4$ and $CdFe_2O_4$ are necessitated to validate the theoretical anisotropic effects in momentum densities (Fig. 6).

The difference in CPs between convoluted theoretical (LCAO–DFT–LDA, LCAO–DFT–GGA,

**Figure 4** Majority-spin (↑) and minority-spin (↓) density of states (DOS) for **a** 3*d* and 4*s* states of Zn, **b** 3*d* and 4*s* states of Fe, **c** 2*s* and 2*p* states of O and **d** total ZnFe₂O₄ using LCAO–B3LYP approximation.
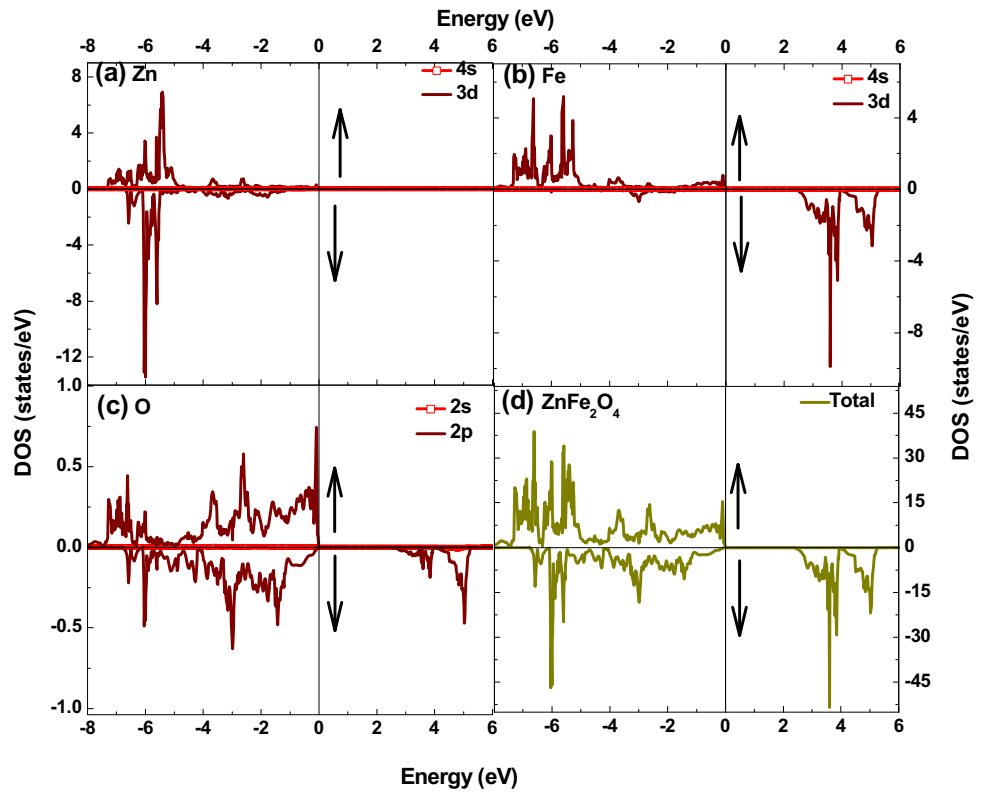


**Figure 5** Majority-spin (↑) and minority-spin (↓) density of states (DOS) for **a** 4*d* and 5*s* states of Cd, **b** 3*d* and 4*s* states of Fe, **c** 2*s* and 2*p* states of O and **d** total CdFe₂O₄ using LCAO–B3LYP approximation. The range of DOS is different than that in energy bands for a clear visualization.
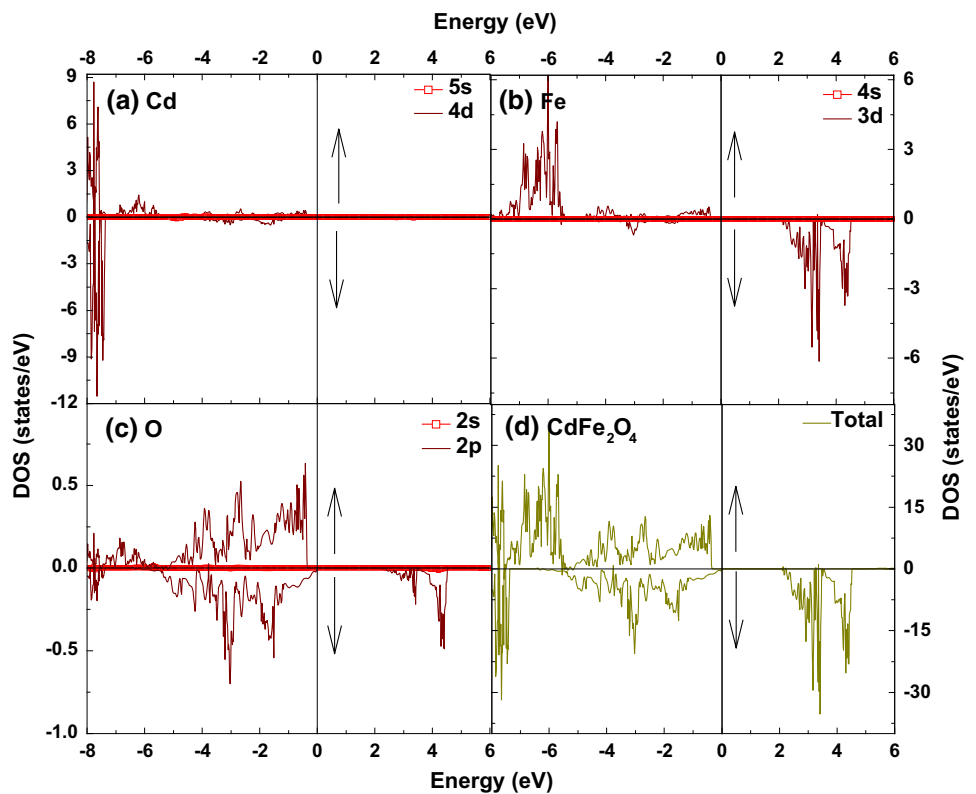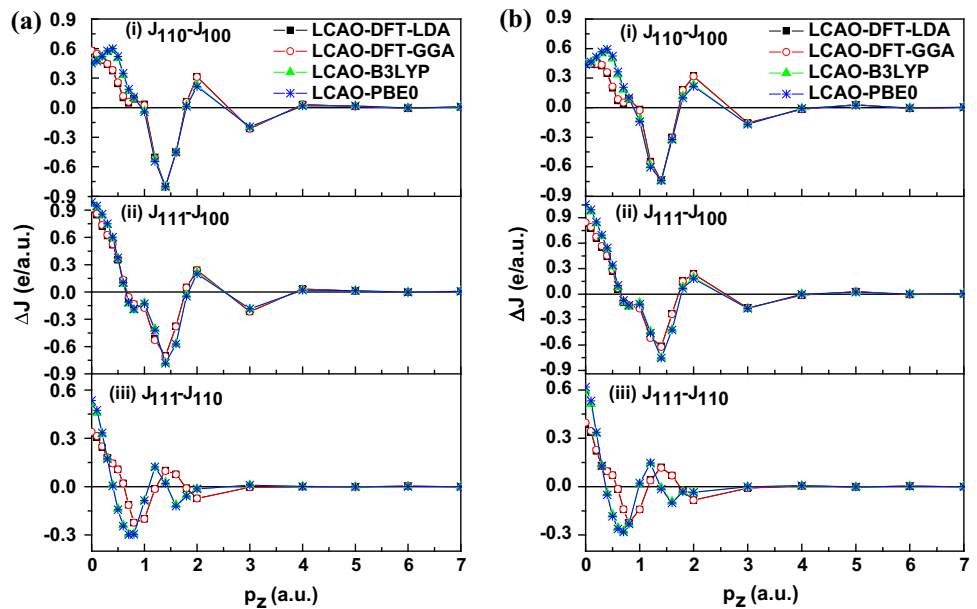
**Figure 6** Anisotropies in the unconvoluted theoretical Compton profiles of **a** ZnFe$_2$O$_4$ and **b** CdFe$_2$O$_4$ calculated using LCAO–DFT–LDA, LCAO–DFT–GGA, LCAO–B3LYP and LCAO–PBE0 approximations for the directional pairs (i) $J_{110}$–$J_{100}$, (ii) $J_{111}$–$J_{100}$ and (iii) $J_{111}$–$J_{110}$. The solid lines are drawn for a quick view of trend.



LCAO–B3LYP and LCAO–PBE0) and experimental data have been plotted in Fig. 7a, b for ZnFe$_2$O$_4$ and CdFe$_2$O$_4$, respectively. The numerical values of unconvoluted theoretical (LCAO–DFT–LDA, LCAO–DFT–GGA, LCAO–B3LYP and LCAO–PBE0) and experimental CPs for ZnFe$_2$O$_4$ and CdFe$_2$O$_4$ (with statistical errors) have been collated in Tables 3 and 4, respectively. In Tables 3 and 4, total CPs for each approximation is calculated by adding the FA core CP contribution [35] to the respective LCAO-based CP data of valence electrons. Also, to mimic experimental resolution, each theoretical data is convoluted with fwhm of 0.34 a.u. (momentum resolution of present experimental setup) before taking the difference between theoretical and experimental CPs. From Tables 3, 4 and Fig. 7a, b, it is observed that experimental CP data of both the compounds underestimate the momentum densities in the low momentum region ($p_z \leq 1.0$. a.u.). This trend reverses in the region $1.0 \leq p_z \leq 4.0$ a.u. Also, the difference in the higher momentum region ($p_z \geq 4.0$. a.u.) is very small (within the experimental error) for CdFe$_2$O$_4$. Such trend in high momentum region is expected because of contribution of core electrons whose wave functions are well defined by HF approximation. For quantitative conclusions related to goodness of agreement between theoretical CP with the experimental data for both the compounds, we have
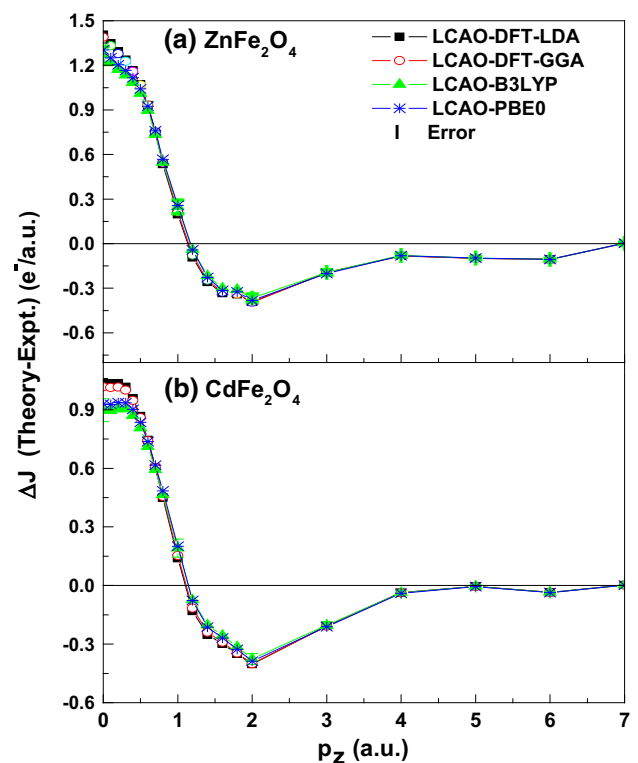


**Figure 7** Different profiles deduced from isotropic convoluted theoretical (LCAO–DFT–LDA, LCAO–DFT–GGA, LCAO–B3LYP and LCAO–PBE0 approximations) and experimental Compton profiles for **a** ZnFe$_2$O$_4$ and **b** CdFe$_2$O$_4$. The solid lines are drawn for a quick view of trend.

undertaken $\chi^2$ fitting. For this purpose, we have used the following formula,

$$\chi^2 = \sum_{p_z=0}^{7} \left[ \frac{J^{\text{LCAO–DFT–LDA/LCAO–DFT–GGA/LCAO–B3LYP/LCAO–PBE0}}(p_z) - J^{\text{Experiment}}(p_z)}{\sigma(p_z)} \right]^2 \qquad (6)$$

Here, $\sigma(p_z)$ is the statistical error at each $p_z$ value. The $\chi^2$ value for $ZnFe_2O_4$ ($CdFe_2O_4$) using LCAO–DFT–LDA, LCAO–DFT–GGA, LCAO–B3LYP and LCAO–PBE0 approximations are computed as 4540.14 (2847.40), 4484.60 (2776.84), 3951.46 (2356.82) and 4189.12 (2534.73), respectively. Hence, the lowest value of $\chi^2$ indicates an overall better agreement by LCAO–B3LYP scheme for both the compounds. Further similar type of performance of both the hybridized approximations (LCAO–B3LYP and LCAO–PBE0) is due to an incorporation of HF exchange effects in such computations. The difference in LCAO–B3LYP and LCAO–PBE0 data may be due to the different contribution of hybridization in exchange and correlation potentials and the percentage of mixing of HF with DFT (being 20 and 25% in B3LYP and PBE0 schemes). In the low momentum side differences between theoretical and experimental CPs may be due to non-inclusion of relativistic effects and Lam–Platzman (LP) correlation [19] in LCAO calculations and further possibility for improvement in the quality of Gaussian basis sets used in the present computations.

## EVED

To highlight relative nature of bonding in the present iso-electronic compounds, we have rescaled the

**Table 3** Unconvoluted theoretical (LCAO–DFT–LDA, LCAO–DFT–GGA, LCAO–B3LYP and LCAO–PBE0) and experimental Compton profiles along with statistical errors ($\pm \sigma$) for $ZnFe_2O_4$

| $p_z$ (a.u.) | $J(p_z)$ (e/a.u.) | | | | |
|---|---|---|---|---|---|
| | Theory | | | | Expt. |
| | LCAO–DFT–LDA | LCAO–DFT–GGA | LCAO–B3LYP | LCAO–PBE0 | |
| 0.0 | 26.136 | 26.117 | 25.996 | 26.029 | 24.659 ± 0.058 |
| 0.1 | 26.098 | 26.080 | 25.960 | 25.993 | 24.571 ± 0.058 |
| 0.2 | 25.831 | 25.816 | 25.700 | 25.734 | 24.341 ± 0.057 |
| 0.3 | 25.394 | 25.382 | 25.280 | 25.314 | 23.954 ± 0.057 |
| 0.4 | 24.728 | 24.719 | 24.643 | 24.676 | 23.407 ± 0.056 |
| 0.5 | 23.955 | 23.950 | 23.900 | 23.932 | 22.714 ± 0.054 |
| 0.6 | 22.990 | 22.988 | 22.953 | 22.982 | 21.905 ± 0.053 |
| 0.7 | 21.878 | 21.882 | 21.858 | 21.884 | 21.003 ± 0.052 |
| 0.8 | 20.621 | 20.630 | 20.631 | 20.653 | 20.014 ± 0.050 |
| 1.0 | 17.952 | 17.968 | 18.018 | 18.030 | 17.772 ± 0.046 |
| 1.2 | 15.341 | 15.357 | 15.395 | 15.392 | 15.540 ± 0.042 |
| 1.4 | 13.143 | 13.155 | 13.183 | 13.170 | 13.484 ± 0.038 |
| 1.6 | 11.248 | 11.254 | 11.281 | 11.265 | 11.678 ± 0.035 |
| 1.8 | 9.718 | 9.720 | 9.751 | 9.735 | 10.134 ± 0.031 |
| 2.0 | 8.468 | 8.467 | 8.495 | 8.480 | 8.920 ± 0.029 |
| 3.0 | 4.794 | 4.791 | 4.793 | 4.785 | 5.002 ± 0.018 |
| 4.0 | 3.006 | 3.006 | 3.010 | 3.007 | 3.099 ± 0.012 |
| 5.0 | 2.092 | 2.091 | 2.093 | 2.092 | 2.193 ± 0.010 |
| 6.0 | 1.542 | 1.542 | 1.543 | 1.543 | 1.651 ± 0.007 |
| 7.0 | 1.167 | 1.167 | 1.167 | 1.167 | 1.183 ± 0.005 |

J Mater Sci (2020) 55:3912–3925

**Table 4** Unconvoluted theoretical (LCAO–DFT–LDA, LCAO–DFT–GGA, LCAO–B3LYP and LCAO–PBE0) and experimental Compton profiles along with statistical errors ($\pm\ \sigma$) for $CdFe_2O_4$

| $p_z$ (a.u.) | $J(p_z)$ (e/a.u.) | | | | |
|---|---|---|---|---|---|
| | Theory | | | | Expt. |
| | LCAO–DFT–LDA | LCAO–DFT–GGA | LCAO–B3LYP | LCAO–PBE0 | |
| 0.0 | 28.354 | 28.329 | 28.211 | 28.243 | $27.237 \pm 0.059$ |
| 0.1 | 28.308 | 28.285 | 28.162 | 28.194 | $27.089 \pm 0.059$ |
| 0.2 | 28.042 | 28.021 | 27.897 | 27.929 | $26.792 \pm 0.058$ |
| 0.3 | 27.586 | 27.569 | 27.460 | 27.492 | $26.347 \pm 0.058$ |
| 0.4 | 26.874 | 26.861 | 26.784 | 26.816 | $25.750 \pm 0.056$ |
| 0.5 | 26.051 | 26.042 | 25.997 | 26.027 | $25.008 \pm 0.055$ |
| 0.6 | 25.039 | 25.035 | 25.006 | 25.034 | $24.128 \pm 0.054$ |
| 0.7 | 23.859 | 23.861 | 23.844 | 23.869 | $23.123 \pm 0.052$ |
| 0.8 | 22.534 | 22.542 | 22.550 | 22.570 | $22.009 \pm 0.050$ |
| 1.0 | 19.726 | 19.742 | 19.793 | 19.802 | $19.599 \pm 0.046$ |
| 1.2 | 16.961 | 16.978 | 17.019 | 17.015 | $17.192 \pm 0.042$ |
| 1.4 | 14.589 | 14.602 | 14.637 | 14.625 | $14.918 \pm 0.038$ |
| 1.6 | 12.502 | 12.510 | 12.546 | 12.532 | $12.898 \pm 0.034$ |
| 1.8 | 10.789 | 10.793 | 10.825 | 10.812 | $11.221 \pm 0.031$ |
| 2.0 | 9.386 | 9.387 | 9.412 | 9.400 | $9.854 \pm 0.028$ |
| 3.0 | 5.317 | 5.315 | 5.319 | 5.312 | $5.543 \pm 0.017$ |
| 4.0 | 3.555 | 3.554 | 3.554 | 3.552 | $3.601 \pm 0.012$ |
| 5.0 | 2.646 | 2.646 | 2.647 | 2.645 | $2.653 \pm 0.009$ |
| 6.0 | 2.042 | 2.042 | 2.042 | 2.041 | $2.079 \pm 0.007$ |
| 7.0 | 1.587 | 1.587 | 1.587 | 1.587 | $1.609 \pm 0.006$ |

LCAO–B3LYP-based CP and experiment profile on EVED ($p_z/p_F$) parameters (Fig. 8). Values of Fermi momentum ($p_F$) for $ZnFe_2O_4$ and $CdFe_2O_4$ were taken as 1.48 and 1.42 a.u., respectively. The outer electrons configurations of Zn (Cd), Fe and O atoms in $TMFe_2O_4$ (TM = Zn and Cd) environment are considered as $3d^{10}4s^2$ ($4d^{10}5s^2$), $3d^64s^2$ and $2s^22p^4$, respectively. Since the total valence electrons in both the iso-electronic compounds are 52, therefore each EVED profile has been normalized to 26 $e^-$ in the major $p_z$ range of 0–2 a.u. From Fig. 8, EVED ($p_z/p_F = 0$) value of $CdFe_2O_4$ using LCAO–B3LYP (experiment) is found to be 2.61 (0.76) % lesser than that of $ZnFe_2O_4$. Such a trend indicates more ionic (or less covalent) character of $CdFe_2O_4$ than $ZnFe_2O_4$. This is admittedly due to a fact that the lower value of $J(p_z/p_F = 0.0)$ indicates the lesser sharing of the electrons along the bond directions which further leads to lesser covalent (or higher ionic) character in the compound. Trend shown by present theoretical (B3LYP) and experimental EVED profiles is also in accordance with earlier discussed MP and OP analysis. Such type of confirmation of charge transfer and

overlap populations (as deduced from MP analysis) was also quite successful in other compounds like $TMWO_4$ (TM = Zn and Cd) [37], $Ag_2TMO_4$ (TM = Cr and Mo) [38] and $TMTiO_3$ (TM = Ba, Sr and Ca) [39].

## LCAO-based magnetization

Local magnetic moments for Fe ions in $ZnFe_2O_4$ ($CdFe_2O_4$) have been calculated using LCAO–DFT–LDA, LCAO–DFT–GGA, LCAO–B3LYP and LCAO–PBE0 schemes and the values are found to be 3.47 (3.87), 3.99 (4.07), 4.24 (4.24) and 4.31 (4.32) $\mu_B$ per formula unit, respectively. Here, the unit cell magnetic moment for $ZnFe_2O_4$ ($CdFe_2O_4$) are also calculated as 7.87 (9.23), 9.57 (9.93), 9.99 (9.99) and 10.01 (10.01) $\mu_B$ from LCAO–DFT–LDA, LCAO–DFT–GGA, LCAO–B3LYP and LCAO–PBE0 schemes, respectively. Our LCAO–B3LYP formulation-based magnetic moments of Fe ions for both the ferrites are in accordance with the available data [3, 8, 9, 12–14]. In case of LCAO–B3LYP, the magnetic moment of Fe ions is approximately equal to the experimental value of 4.22 $\mu_B$. Also, our unit cell magnetic moment using
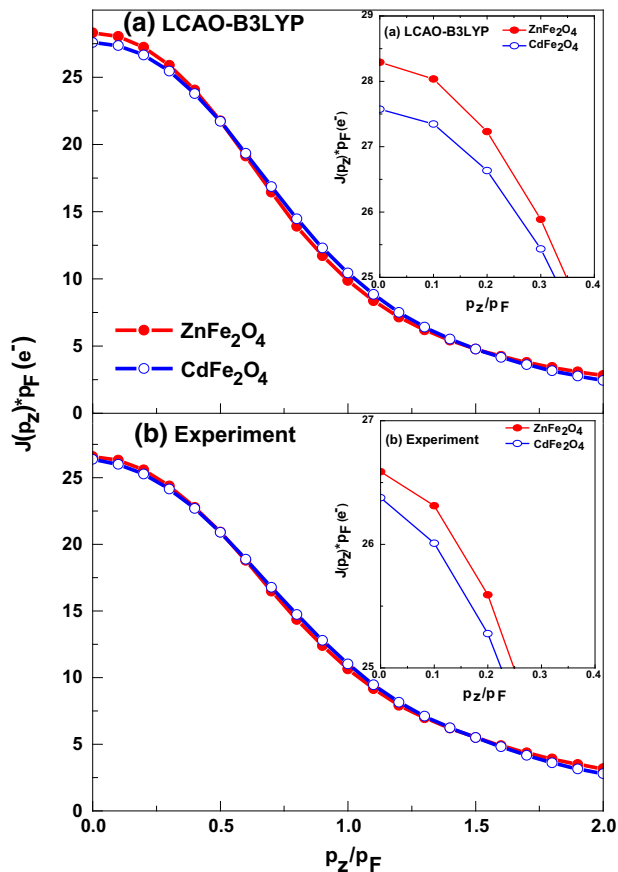
🔵 Springer

**Figure 8** Equal-valence-electron-density (EVED) profiles of iso-electronic $ZnFe_2O_4$ and $CdFe_2O_4$ for **a** LCAO–B3LYP and **b** experimental. In the inset, the values of $J(p_z/p_F)$ near $p_z/p_F = 0$ are shown.

LCAO–B3LYP scheme for $ZnFe_2O_4$ is found to be same as reported by Soliman et al. [8] using FP-LAPW approach.

## Conclusions

MP analysis, energy bands, DOS, band gaps and CPs computed using DFT–LDA, DFT–GGA, B3LYP and PBE0 within LCAO approximations along with Compton profile measurements for $ZnFe_2O_4$ and $CdFe_2O_4$ are presented. Further, MP analysis shows the charge transfer from zinc/cadmium and iron to oxygen atoms. On the basis of EVED CPs and MP data, more ionic character in $CdFe_2O_4$ than that in $ZnFe_2O_4$ was observed. The magnetic moments are well explored by the LCAO–B3LYP approximation. A closer agreement of LCAO–B3LYP-based Compton profiles with the experimental CPs, reproducibility of

band gaps, confirmation of trend of B3LYP-based MP and OP data together with electronic response and magnetization data unambiguously warrants use of hybrid functionals for exchange and correlation potentials in the spinel ferrites, as reported here.

## Compliance with ethical standards

**Conflict of interest** The authors declare that they have no conflict of interest.

## References

[1] Evans BJ, Hafner SS, Weber HP (1971) Electric field gradients at $^{57}$Fe in $ZnFe_2O_4$ and $CdFe_2O_4$. J Chem Phys 55:5282–5288

[2] Pasquevich AF, Shitu J (1999) PAC study of $CdFe_2O_4$ and $ZnFe_2O_4$. Hyperfine Interact 120(121):463–468

[3] Cheng C (2008) Long-range antiferromagnetic interactions in $ZnFe_2O_4$ and $CdFe_2O_4$: density functional theory calculations. Phys Rev B 78:132403-1–132403-4

[4] Cheng C, Liu C-S (2009) Effects of cation distribution in $ZnFe_2O_4$ and $CdFe_2O_4$: ab initio studies. J Phys Conf Ser 145:012028-1–012208-4

[5] Pénicaud M, Siberchicot B, Sommers CB, Kübler J (1992) Calculated electronic band structure and magnetic moments of ferrites. J Magn Magn Mater 103:212–220

[6] Singh DJ, Gupta M, Gupta R (2001) Density-functional description of spinel $ZnFe_2O_4$. Phys Rev B 63:205102–1–205102-5

[7] Yao J, Li X, Li Y, Le S (2013) Density functional theory investigations on the structure and electronic properties of normal spinel $ZnFe_2O_4$. Integr Ferroelectr 145:17–23

[8] Soliman S, Elfalaky A, Fecher GH, Felser C (2011) Electronic structure calculations for $ZnFe_2O_4$. Phys Rev B 83:085205-1–085205-6

[9] Schiessl W, Potzel W, Karzel H, Steiner M, Kalvius GM, Martin A, Krause MK, Halevy I, Gal J, Schäfer W, Will G, Hillberg M, Wäppling R (1996) Magnetic properties of the $ZnFe_2O_4$ spinel. Phys Rev B 53:9143–9152

[10] Cross WB, Affleck L, Kuznetsov MV, Parkin IP, Pankhurst QA (1999) Self-propagating high-temperature synthesis of ferrites $MFe_2O_4$ (M = Mg, Ba Co, Ni, Cu, Zn); reactions in an external magnetic field. J Mater Chem 9:2545–2552

[11] Rama Krishna K, Ravinder D, Vijaya Kumar K, Abraham Lincon Ch (2012) Synthesis, XRD and SEM studies of zinc substitution in nickel ferrites by citrate gel technique. World J Condens Matter Phys 2:153–159

[12] Quintero JM, Rodríguez KLS, Pasquevich GA, Zélis PM, Stewart SJ, Torres CER, Errico LA (2016) Experimental and ab initio study of the hyperfine parameters of $ZnFe_2O_4$ with defects. Hyperfine Interact 237:63-1–63-7

[13] Quintero JJM, Rodríguez KLS, Torres CER, Errico LA (2019) Ab initio study of the role of defects on the magnetic response and the structural, electronic and hyperfine properties of $ZnFe_2O_4$. J Alloys Compd 775:1117–1128

[14] Mahmood Q, Yaseen M, Bhamu KC, Mahmood A, Javed Y, Ramay SM (2018) Magnetism, optical, and thermoelectric response of $CdFe_2O_4$ by using DFT scheme. Chin Phys B 27:037103-1–037103-8

[15] Nikumbh AK, Nagawade AV, Gugale GS, Chaskar MG, Bakare PP (2002) The formation, structural, electrical, magnetic and Mössbauer properties of ferrispinels, $Cd_{1-x}$-$Ni_xFe_2O_4$. J Mater Sci 37:637–647

[16] Kamazawa K, Park S, Lee S-H, Sato TJ, Tsunoda Y (2004) Dissociation of spin objects in geometrically frustrated $CdFe_2O_4$. Phys Rev B 70:024418-1–024418-5

[17] Noor S, Rahman MM, Sikder SS, Hakim MA (2011) Effect of Cd substitution on structural and transport properties of Co-ferrites. Jahangirnagar Univ J Sci 34:1–11

[18] Zaari H, El Hachimi AG, Benyoussef A, El Kenz A (2015) Comparative study between TB-mBJ and GGA + U on magnetic and optical properties of $CdFe_2O_4$. J Magn Magn Mater 393:183–187

[19] Cooper MJ, Mijnarends PE, Shiotani N, Sakai N, Bansil A (2004) X-ray Compton scattering. Oxford Science Publications, Oxford University Press, New York **(and references therein)**

[20] Heda NL, Ahuja BL (2010) Role of *in-house* Compton spectrometer in probing the electronic properties. In: Ahuja BL (ed) Recent trends in radiation physics research. Himanshu Publications, New Delhi, pp 25–30

[21] Dovesi R, Saunders VR, Roetti C, Orlando R, Zicovich-Wilson CM, Pascale F, Civalleri B, Doll K, Harrison NM, Bush IJ, D'Arco Ph, Llunell M, Causa M, Neol Y (2014) CRYSTAL14 User's manual. University of Torino, Torino **(and references therein)**

[22] Perdew JP, Zunger A (1981) Self-interaction correlation to density functional approximations for many-electron systems. Phys Rev B 23:5048–5079

[23] Perdew JP, Ruzsinszky A, Csonka GI, Vydrov OA, Scuseria GE, Constantin LA, Zhou X, Burke K (2008) Restoring the density-gradient expansion for exchange in solids and surfaces. Phys Rev Lett 100:136406-1–136406-4

[24] Muscat J, Klauber C (2001) A combined ab initio and photoelectron study of galena (PbS). Surf Sci 491:226–238

[25] Adamo C, Barone V (1999) Toward reliable density functional methods without adjustable parameters: the PBE0 model. J Chem Phys 110:6158–6170

[26] Becke AD (1988) Density-functional exchange-energy approximation with correct asymptotic behavior. Phys Rev A 38:3098–3100

[27] Perdew JP, Burke K, Ernzerhof M (1996) Generalized gradient approximation made simple. Phys Rev Lett 77:3865–3868

[28] Lee C, Yang W, Parr RG (1988) Development of Colle–Salvetti correlation-energy formula into a functional of the electron density. Phys Rev B 37:785–789

[29] Vosko SH, Wilk L, Nusair M (1980) Accurate spin-dependent electron liquid correlation energies for local spin density calculations: a critical analysis. Can J Phys 58:1200–1211

[30] http://www.crystal.unito.it/basis-sets.php. Accessed 3 Sept 2019

[31] Kokalj A (2003) Computer graphics and graphical user interfaces as tool in simulations of matter at the atomic scale. Comput Mater Sci 28:155–168

[32] Ahuja BL, Sharma M, Mathur S (2006) Anisotropy in the momentum density of tantalum. Nucl Instrum Methods B 244:419–426

[33] Timms DN (1989) Compton scattering studies of spin and momentum densities. (Unpublished Ph.D. thesis), University of Warwick, UK

[34] Felsteiner J, Pattison P, Cooper MJ (1974) Effect of multiple scattering on experimental Compton profiles: a Monte-Carlo calculation. Philos Magn 30:537–548

[35] Biggs F, Mendelsohn LB, Mann JB (1975) Hartree–Fock Compton profiles. At Data Nucl Data Tables 16:201–308

[36] Meena BS, Heda NL, Kumar K, Bhatt S, Mund HS, Ahuja BL (2016) Compton profiles and Mulliken's populations of cobalt, nickel and copper tungstates: experiment and theory. Phys B 484:1–6

[37] Meena BS, Heda NL, Mund HS, Ahuja BL (2015) Compton profiles and electronic structure of monoclinic zinc and cadmium tungstates. Radiat Phys Chem 117:93–101

[38] Meena SK, Heda NL, Arora G, Meena L, Ahuja BL (2019) Performance of hybrid exchange–correlation potential for photocatalytic silver chromate and molybdate: LCAO theory and Compton spectroscopy. Physica B 560:236–243

[39] Meena SK, Dashora A, Heda NL, Ahuja BL (2019) Compton spectroscopy and electronic structure study for tetragonal barium titanate. Radiat Phys Chem 158:46–52

[40] Fritsch D (2018) Electronic and optical properties of spinel zinc ferrite: ab initio hybrid functional calculations. J Phys Condens Matter 30:095502-1–095502-5

[41] Valenzuela MA, Bosch P, Jiménez-Becerrill J, Quiroz O, Páez AI (2002) Preparation, characterization and photocatalytic activity of ZnO, $Fe_2O_3$ and $ZnFe_2O_4$. J Photochem Photobiol A Chem 148:177–182

[42] Akamatsu H, Zong Y, Fujiki Y, Kamiya K, Fujita K, Murai S, Tanaka K (2008) Structural and magnetic properties of $CdFe_2O_4$ thin films fabricated via sputtering method. IEEE Trans Magn 44:2796–2799